A First Principle Study of Optoelectronic, Thermoelectric, and Mechanical Properties of Ca_2VInO_6 Double Perovskite

Roll: 191306
Session: 2019–2020

Report submitted to the Department of Physics at
Jashore University of Science and Technology
in partial fulfillment of the requirements
for the degree of Bachelor of Science
with Honours in Physics

May 2025

Abstract

In this work, we computationally explored the structural, mechanical, electronic, optical and thermoelectric properties of Ca_2VInO_6 oxide double provskites using the full potential linearized augmented plane wave (FP-LAPW) method, based on density functional theory method, as implemented in the WIEN2k package. The compound have a perfect cubic symmetry with space group $Fm\bar{3}m$ (space group no: 225). The mechanical properties show that Ca_2VInO_6 is ductile in nature. The analysis of electronic properties reveal that Ca_2VInO_6 exhibit an indirect bandgap, with values of 2.362 eV. The optical properties are investigated through the dielectric function, absorption coefficient, optical conductivity, reflectivity and refractive index. These properties demonstrate a significant response in the ultraviolet and visible regions, making the material suitable for photocell and optoelectronic device applications. Finally, thermoelectric properties such as power factor, electrical conductivity, thermal conductivity, Seebeck coefficient and figure of merit were calculated using BoltzTraP code. At room temperature, the estimated values of the figure of merit is 0.83 for Ca_2VInO_6. This value indicate that Ca_2VInO_6 is a promising candidate for thermoelectric device applications.

Acknowledgements

Firstly, I praise and thank almighty Allah, the Lord of the worlds, the Most Merciful, the Guider of hearts, the Provider of sustenance, the Owner of life and death.

I would like to thank my supervisor Dr. Mohammad Abdur Rashid, for his constant supervision, guidance and patience to complete my project properly. I appreciate all the faculty members of Department of Physics. I want to express my gratitude to the Quantum Materials Simulation Lab (QMSL) members who supported me throughout the project, both directly and indirectly. Besides, I have received many facilities from QMSL, including computational facilities and printing services.

On a personal note, I would like to thank my parents and grandmother for their sacrifice and support over the years. Their love and encouragement always give me mental support to continue my study smoothly.

Contents

List of Figures

List of Tables

A First Principle Study of Optoelectronic, Thermoelectric, and Mechanical Properties of Ca_2VInO_6 Double Perovskite

Chapter 1

Introduction

Energy is a basic component of society which has a key role in its development by upgrading the standards and quality of human life's. Nowdays energy crisis is a major concern of researchers globally because the energy resources are depleting continuously, which is also not sound ecologically. Fossile fuels are the primary resources of our energy demand but they are non-renewable and limited in supply. According to some estimations, they will be consumed within the next five decades [1]. The rapid increase in energy demand has motivated the scientific community to look for smart and technologically advanced devices which can harvest enegy from natural sources like the sun, wind and tides [2, 3]. Sun is one of the biggest sources of heat and light which could be converted into electrical energy using suitable optoelectronic and thermoelectric devices [4]. The efficiency of any such device depends upon the underlying material in these devices. Double perovskite materials have the potential to harvest solar energy. In recent years, double perovskite materials have attracted much attention due to their promising applications in various fields, such as light-emitting diode (LEDs), lasers, radiation detectors, and solar cells [5–9].

Among different types of double perovskites, lead-based DP materials exhibit exceptional applications in photovoltaic technologies which are due to their suitable direct band gap, high absorption properties, high carrier mobility and charge diffu-

sion, and small effective masses [10–13]. Although lead-based DP possess remarkable characteristics as mentioned earlier, most of the efficient perovskites explored yet contain the lead element which is very toxic and badly affects the reproductive and nervous systems of the human body [14]. Therefore, in recent years, finding stable and nature-frendly and non-toxic DP materials has been considered as a stategically important field of study. In this regard, lead-free halides and double perovskites oxides in which lead is replaced by silver (Ag), bismuth (Bi), and so on have attracted great research interest from theoretical and experimental perspectives. It has been indicated that the high optical conductivity, low reflectivity, and high absorption coefficients of this family of materials make them promising materials for use in many practical applications [15–31].

Double perovskites are represented by the general chemical formula $A_2BB'X_6$ in which B and B′ represent monovalent (B^{1+}) and trivalent (B^{3+}) cations, respectively. They are named as double perovskites because their unit cell is twich that of the simple perovskites. Generally, A-site cation belongs to alkali metals (like K, Cs, Rb etc), B and B′ cations are transition metals (like Ag, Pd, Pt etc) while X is halides or oxygen [32]. As the power conversion efficiency has increased steadily and explosively from 3.8% in 2009 to 25.7% at present [33, 34], oxide-based double perovskite materials have got dramatic attention in the research community for photovoltaic and thermoelectric applications. For examples, Kazim et al. [35] have done the first principle study of wide band gap semiconducting materials Ba_2ZrCeO_6 and Ba_2ZrTiO_6 and have revealed that these materials exhibit optimal optoelectronics properties for incident light in the UV region and act as high-potential thermoelectric materials at high temperature. Aziz et al. [36] estimated the properties of X_2NaIO_6 (X= Pb,Sr) and revealed that both Sr_2NaIO_6 and Pb_2NaIO_6 exhibited good semiconducting behaviours with direct bandgaps (E_g) of 5.48 and 3.75 eV, respectively. In addition, Sr_2NaIO_6 acheived a higher ZT value and power factor (PF) of 0.7728 and 206.3, respectively. In addition, cubic X_2NaIO_6 was more suitable in thermoelectric (TE) applications and optoelectronic devices. Al-Qaisi et al. [37] have investigated elastically stable, anisotropic, and brittle Ba_2NaIO_6 double perovskite direct and narrow bandgap semiconductor material for optoelectronic and

thermoelectric materials using DFT approach. Apart from that, Khandy et al. [38] analyzed the physical characteristics of Ba_2CdReO_6. The study found that the compound displayed a minimal stability energy curve in the ferromagnetic (FM) setup, while the half-metallic feature was observed in the band structure. Moreover, the physical attributes of the material were the major advantages that allowed it to be widely utilized as an electrode material in spintronics applications.

Motivated by the attractive characteristics of oxide-based double perovskites, we have used a first-principle approach and density functional theory (DFT) as implemented in WIEN2k [39, 40] code to study the structural, electrical, optical, thermoelectric and mechanical properties of Ca_2VInO_6. Density Functional Theory (DFT) [41,42] is a computational approach employed in quantum mechanics for characterizing the electronic structure and characteristics of solid materials. WIEN2k stands out as a versatile and advanced software package designed for electronic structure calcualtions in the field of materials science. It uses the full-potential linearized augmented plane wave (FP-LAPW) method. Transport properties were calculated using the BoltzTraP code [43], where we computed thermal and electrical conductivities, the Seebeck coefficient and the power factor. BoltzTraP is a program that computes semiclassical transport coefficients using smoothed Fourier interpolation of electronic bands.

Chapter 2 presents the fundamental principles of quantum mechanics that serve as the theoretical foundation for density functional theory (DFT). The chapter begins with the time-independent Schrödinger equation and discusses the criteria for determining the ground-state wave function. It also includes a brief overview of the Born–Oppenheimer approximation and the Hartree–Fock method, along with its limitations. The theoretical framework of DFT is then introduced and discussed in detail. Chapter 3 explores the structural, electronic, optical, thermoelectric, and mechanical properties of Ca_2VInO_6. Finally, in Chapter 4, we summarize the key findings and highlight the potential applications of the material based on its analyzed properties.

Chapter 2

Theory

2.1 Basic Quantum Mechanics

A proper understanding of Density Functional Theory (DFT) begins with the fundamental principles of quantum mechanics, which describe the behavior of matter at atomic and subatomic scales. Central to this theory is the Schrödinger equation, which governs the quantum states of physical systems and enables the determination of wave functions and energy levels. The Schrödinger equation can be expressed in both time-dependent and time-independent forms. We will focus on the time-independent Schrödinger equation, which is particularly relevant for stationary states of quantum systems. Solutions to the time-independent Schrödinger equation provide the probability distribution of particles and the corresponding energy eigenvalues, offering crucial insights into the electronic structure of atoms and molecules.

2.1.1 Schrödinger Equation

The Schrödinger equation is a key equation in quantum mechanics that characterizes the quantum state of a system. It is fundamental for understanding the behavior of particles at atomic and subatomic levels, such as electrons, photons, and other

quantum entities [44]. First introduced by Erwin Schrödinger in 1925, the equation offers a mathematical framework to predict the properties and dynamics of quantum systems.. The mathematical form of the Schrödinger equation is

$$\hat{H}\Psi = E\Psi \tag{2.1}$$

where, $\hat{H}$ is the Hamiltonian operator, Ψ is the wave function of the system, and E is the energy eigenvalue corresponding to the quantum state described by Ψ. This equation is crucial in finding the stationary states of quantum systems. The Hamiltonian, $\hat{H}$, represents the total energy operator of the system and is typically composed of two parts: the kinetic energy operator, $\hat{T} = -\frac{\hbar^2}{2m}\nabla^2$ and the potential energy operator, $\hat{V} = V(\mathbf{r})$. The kinetic energy operator describes the motion of particles, while the potential energy operator accounts for the forces acting on them due to their positions within the system. Together, these components determine the total energy of the quantum system. Hence, the Schrödinger equation in three dimensions becomes

$$E\Psi(\mathbf{r}) = \left[-\frac{\hbar^2}{2m}\nabla^2 + V(\mathbf{r}) \right]\Psi(\mathbf{r}). \tag{2.2}$$

2.1.2 Wave Functions and Probability Density

The wave function, $\Psi(\mathbf{r})$, is a key concept in quantum mechanics that encodes all information about a system's quantum state. It describes the probability of finding particles at specific positions $\mathbf{r}$ and with particular properties. Although Ψ itself does not have direct physical meaning, it is essential for calculating observable quantities like energy and determining the probability distribution of particle positions, $|\Psi|^2$, which provides insights into their behavior within the system [45].

2.2 The Many-Body Problem

The many-body problem in quantum mechanics concerns the difficulty of describing systems made up of multiple interacting particles. While single-particle systems can

often be solved analytically, many-body systems involve complex interactions that lead to phenomena like correlations and collective behaviors. The Hamiltonian for a many-body system that includes both nuclei and electrons can be expressed as [46].

$$\hat{H} = \hat{T}_{nuclei} + \hat{T}_{electrons} + \hat{V}_{nn} + \hat{V}_{ee} + \hat{V}_{ne} \tag{2.3}$$

with the terms representing:

- $\hat{T}_{nuclei}$: the kinetic energy of the nuclei,
- $\hat{T}_{electrons}$: the kinetic energy of the electrons,
- $\hat{V}_{nn}$: the nucleus-nucleus Coulomb repulsion,
- $\hat{V}_{ee}$: the electron-electron Coulomb repulsion,
- $\hat{V}_{ne}$: the attractive interaction between nuclei and electrons.

These interaction terms make solving the Schrödinger equation for large systems of atoms exceedingly complex. The Coulomb interactions $\hat{V}_{nn}$, $\hat{V}_{ee}$ and $\hat{V}_{ne}$ describe the forces between particles, which must be accounted for when determining the total energy of the system. As the number of atoms increases, the number of interactions grows rapidly, making direct analytical or numerical solutions impractical. With the explicit forms of the kinetic energies and interaction terms, the many-body Hamiltonian for a system consisting of nuclei and electrons becomes:

$$\hat{H} = -\sum_I \frac{\hbar^2}{2M_I}\nabla^2_{\mathbf{R}_I} - \sum_i \frac{\hbar^2}{2m_e}\nabla^2_{\mathbf{r}_i} + \frac{1}{2}\sum_{I,J}\frac{Z_I Z_J e^2}{|\mathbf{R}_I - \mathbf{R}_J|} + \frac{1}{2}\sum_{i,j}\frac{e^2}{|\mathbf{r}_i - \mathbf{r}_j|} - \sum_{I,i}\frac{Z_I e^2}{|\mathbf{R}_I - \mathbf{r}_i|}. \tag{2.4}$$

Here, the indices I and J run over the nuclei, while i and j run over the electrons. $\mathbf{R}_I$ and M_I are the position and mass of the nuclei, respectively, and $\mathbf{r}_i$ and m_e are the position and mass of the electrons. The terms $|\mathbf{R}_I - \mathbf{R}_J|$, $|\mathbf{R}_I - \mathbf{r}_i|$, and $|\mathbf{r}_i - \mathbf{r}_j|$ represent the distances between nuclei-nuclei, nuclei-electrons, and electrons-electrons, respectively. Z_I is the atomic number of the I-th nucleus.

Solving the many-body Hamiltonian presents several significant challenges in quantum mechanics, particularly in systems involving both electrons and nuclei. The high dimensionality of the problem is a major hurdle; for a system with N electron and M nuclei, the wave function depends on $3(N + M)$ variables, making analytical solutions increasingly intractable as N and M increase. Additionally, the Coulomb interactions between electrons introduce complex correlations, complicating the treatment of each electron as an independent particle. Furthermore, since electrons are fermions, they must adhere to the Pauli exclusion principle, requiring that the many-body wave function is antisymmetric under the exchange of particles, which adds another layer of complexity. The potential energy terms in the Hamiltonian, which encompass nucleus-nucleus and nucleus-electron interactions, further contribute to the difficulty. While analytical solutions are only feasible for very simple systems, such as the hydrogen atom, most many-body systems with multiple electrons and nuclei do not permit exact solutions.

2.2.1 Born-Oppenheimer Approximation

To manage the complexity associated with solving the many-body Hamiltonian in systems comprising both electrons and nuclei, it is essential to adopt simplification strategies. One of the most effective and widely utilized methods is the Born-Oppenheimer approximation. This approach takes advantage of the substantial mass difference between nuclei and electrons, which results in a significant disparity in their respective motion. Since nuclei are much heavier and thus move more slowly than electrons, their positions can be considered fixed while solving the electronic part of the Schrödinger equation. This assumption allows for the separation of the total wave function into independent electronic and nuclear components, thereby reducing the computational burden and simplifying the many-body problem considerably [47].

Under this approximation, the total Hamiltonian can be expressed as a sum of two parts: the electronic Hamiltonian $\hat{H}_{el}$, which describes the motion of electrons in the field of fixed nuclei, and the nuclear Hamiltonian $\hat{H}_{nuc}$, which accounts for the

motion of the nuclei interacting with each other. The total Hamiltonian $\hat{H}$ is then given by:

$$\hat{H} = \hat{H}_{el} + \hat{H}_{nuc} \tag{2.5}$$

where

$$\hat{H} = -\sum_{i} \frac{\hbar^2}{2m_e} \nabla^2_{\mathbf{r}_i} + \frac{1}{2} \sum_{i,j} \frac{e^2}{|\mathbf{r}_i - \mathbf{r}_j|} - \sum_{I,i} \frac{Z_I e^2}{|\mathbf{R}_I - \mathbf{r}_i|}. \tag{2.6}$$

and

$$\hat{H}_{nuc} = \sum_{I} \frac{\hbar^2}{2M_I} \nabla^2_{\mathbf{R}_I} + \frac{1}{2} \sum_{I,J} \frac{Z_I Z_J e^2}{|\mathbf{R}_I - \mathbf{R}_J|}. \tag{2.7}$$

The Born-Oppenheimer approximation simplifies the computational complexity of many-body systems by focusing primarily on the electronic structure. It assumes that the nuclei, being significantly heavier than the electrons, move much more slowly and can therefore be treated as stationary. This allows the electrons to interact within a static potential created by the fixed nuclei. In density functional theory, this approximation is typically employed to reduce the system's complexity. However, if nuclear motion must be included, the Schrödinger equation governing the nuclei's behavior can be solved by treating the nuclei as quantum mechanical objects. The total energy of the system, E_{total}, is then obtained by summing the electronic and nuclear energies, which provides a comprehensive view of the system by accounting for both electronic and nuclear contributions. Once the electronic Hamiltonian $\hat{H}_{el}$ is defined, the electronic Schrödinger equation can be expressed as:

$$\hat{H}_{el} \Psi(\mathbf{r}_1, \mathbf{r}_2, ...\mathbf{r}_N) = E \Psi(\mathbf{r}_1, \mathbf{r}_2, ...\mathbf{r}_N) \tag{2.8}$$

In this equation, $\Psi(\mathbf{r}_1, \mathbf{r}_2, ..., \mathbf{r}_N)$ represents the many-body wave function, depending on the positions of all N electrons, and E is the total energy. Solving the many-body Schrödinger equation is challenging due to the complex dependence of Ψ on all electron coordinates. As N increases, this becomes analytically difficult. Additionally, capturing electron-electron correlations, especially in systems with strong interactions, complicates the problem. While the current approximations work for simple systems like H_2^+, more advanced methods are required for larger systems.

2.2.2 Hartree-Fock Approximation and Its Limitations

The Hartree-Fock approximation is a key method in quantum chemistry used to approximate the many-body wave function of a system of electrons [48]. In this approach, the many-body wave function is represented as a Slater determinant, which ensures the wave function is antisymmetric in accordance with the Pauli exclusion principle. The Slater determinant combines single-particle wave functions (orbitals) for each electron into a single function, ensuring that the overall wave function changes sign when two electrons are exchanged.

Despite its utility, the Hartree-Fock approximation has notable limitations. One significant drawback is its reliance on a mean-field approximation, where each electron moves in an average field created by all other electrons. This assumption overlooks electron correlation effects, which are crucial for accurately describing many-electron systems, particularly in cases involving strong correlations. As a result, the Hartree-Fock method often yields inaccurate results for properties such as bond lengths, reaction energies, and excitation energies.

Moreover, while the Slater determinant correctly handles the antisymmetry of the wave function, it fails to capture the dynamic correlation between electrons that arises from their instantaneous interactions. Additionally, the computational cost of the Hartree-Fock method scales as $O(N^4)$, where N is the number of electrons. This scaling occurs because the method requires calculating integrals over all pairs of electron orbitals. As N increases, the number of required calculations grows rapidly, making the method computationally expensive for larger systems.

2.3 Density Functional Theory

Density Functional Theory (DFT) is a widely used quantum mechanical approach for studying the electronic structure of many-body systems. Instead of relying on complex wave functions, DFT uses electron density as the central variable. This simplification reduces the difficulty of solving the many-body Schrödinger equation. The fundamental idea is that the electron density alone is sufficient to determine

all ground-state properties of a system. DFT is efficient and accurate, making it suitable for exploring large and complex systems. Through the Hohenberg-Kohn theorems and Kohn-Sham equations, DFT offers a practical and reliable framework for analyzing the physical, chemical, and material characteristics of matter.

2.3.1 The Electron Density

In Density Functional Theory (DFT), the electron density $n(\mathbf{r})$ serves as the central variable for describing a quantum system. The electron density represents the probability of finding an electron at a particular point in space and can be derived from the many-body wave function $\Psi(\mathbf{r}_1, \mathbf{r}_2, ...\mathbf{r}_N)$ by integrating over all electron coordinates. This relationship is expressed mathematically as:

$$n(\mathbf{r}) = N \int |\Psi(\mathbf{r}_1, \mathbf{r}_2, ..., \mathbf{r}_N)|^2 d\mathbf{r}_2 d\mathbf{r}_3 ....d\mathbf{r}_N. \tag{2.9}$$

Additionally, we must remember that all electrons are identical; thus, we cannot label them as electron 1 or electron N. Instead, we can determine the probability of any order or set of N electrons being located at the coordinates $\mathbf{r}_1$ to $\mathbf{r}_N$. While the wave function contains comprehensive information about the quantum state of a system, it is the electron density that ultimately determines all measurable properties. The total number of electrons N in the system can also be calculated from the electron density using the equation:

$$N = \int n(\mathbf{r}) d(\mathbf{r}). \tag{2.10}$$

This integration highlights that the electron density encodes vital information about the total number of electrons, making it a fundamental aspect of DFT. By focusing on $n(\mathbf{r})$ instead of the complex multi-dimensional wave function, DFT simplifies calculations, making it a practical and efficient approach for studying the electronic structure of various materials.

2.3.2 Hohenberg-Kohn Theorems

Density Functional Theory (DFT) was formally established in 1964 with the publication of a seminal paper by Hohenberg and Kohn in Physical Review. In this foundational work, the authors introduced two key theorems that form the theoretical basis of all modern DFT approaches. These theorems demonstrated that the ground-state properties of a quantum many-body system are uniquely determined by its electron density, rather than its many-body wave function. This insight provided a new framework for studying quantum systems, offering a more computationally efficient alternative to traditional wave-function-based methods, particularly for large and complex systems.

The Hohenberg-Kohn theorems are central to the formulation of DFT, and they can be summarized as follows:

First theorem: The ground-state electron density $n(\mathbf{r})$ uniquely determines the external potential $V_{ext}(\mathbf{r})$ acting on the electrons. This means that if the electron density of a system is known, the external potential can be uniquely inferred, allowing for the derivation of all ground-state properties, including the total energy, from the electron density.

According to the first theorem, the ground-state density and the external potential correspond in a one-to-one manner. Since the external potential is fixed, the Hamiltonian, and hence the wave function ψ, is determined by the ground-state density $n_0(\mathbf{r})$. The proof of this theorem is straightforward: Consider the ground states of two N-electron systems, characterized by two different external potentials $V_{ext}(\mathbf{r})$ and $V'_{ext}(\mathbf{r})$, which differ by more than an additive constant. The corresponding Hamiltonians, $\hat{H}$ and $\hat{H}'$, would both have the same ground-state density $n(\mathbf{r})$, but different ground-state wave functions, Ψ and Ψ', with $\hat{H}\Psi = E_0\Psi$ and $\hat{H}'\Psi' = E'_0\Psi'$. Since Ψ' is not the ground state of $\hat{H}$, it follows that

$$\begin{aligned} E_0 &< \langle \Psi' | \hat{H} | \Psi' \rangle \\ &< \langle \Psi' | \hat{H}' | \Psi' \rangle + \langle \Psi' | \hat{H} - \hat{H}' | \Psi' \rangle \\ &< E_0' + \int n_0(\mathbf{r}) [V_{ext}(\mathbf{r}) - V_{ext}'(\mathbf{r})] d\mathbf{r} \end{aligned} \tag{2.11}$$

Similarly

$$\begin{aligned} E_0' &< \langle \Psi | \hat{H} | \Psi \rangle \\ &< \langle \Psi | \hat{H} | \Psi \rangle + \langle \Psi | \hat{H}' - \hat{H} | \Psi \rangle \\ &< E_0 + \int n_0(\mathbf{r}) [V_{ext}'(\mathbf{r}) - V_{ext}(\mathbf{r})] d\mathbf{r}. \end{aligned} \tag{2.12}$$

Adding equation (11) and equation (12) leads to the contradiction,

$$E_0 + E_0' < E_0 + E_0' \tag{2.13}$$

Hence, no two different external potentials $V_{ext}(\mathbf{r})$ can give rise to the same ground state density $n_0(\mathbf{r})$ which determines the external potential $V_{ext}(\mathbf{r})$, except for a constant. That is to say, there is a one-to-one mapping between the ground state density $n_0(\mathbf{r})$ and the external potential $V_{ext}(\mathbf{r})$, although the exact formula is unknown.

Second theorem: For any trial electron density $n(\mathbf{r})$, the energy functional $E[n]$ will yield a value that is greater than or equal to the ground-state energy E_0. The equality holds when the trial density corresponds to the true ground-state density. This variational principle implies that one can minimize the energy functional $E[n]$ with respect to the electron density to find the ground state of a system [49].

There exists a universal functional $F[n(\mathbf{r})]$ of the density, independent of the external potential $V_{ext}(\mathbf{r})$, such that the minimum value of the energy functional

$$E[n(\mathbf{r})] \equiv \int n(\mathbf{r}) V_{ext}(\mathbf{r}) d(\mathbf{r}) + F[n(\mathbf{r})] \tag{2.14}$$

yields the exact ground-state energy of the system. The exact ground-state density $n_0(\mathbf{r})$ minimizes this functional. Thus, the exact ground-state energy and density

are fully determined by the functional $E[n(\mathbf{r})]$. The universal functional $F[n(\mathbf{r})]$ can be written as:

$$F[n(\mathbf{r})] \equiv T[n(\mathbf{r})] + E_{int}[n(\mathbf{r})] \tag{2.15}$$

where T[n($\mathbf{r}$)] is the kinetic energy and $E_{int}[n(\mathbf{r})]$ is the interaction energy of the particles. According to the variational principle, for any wave function Ψ', the energy functional

$$E[\Psi'] \equiv \langle \Psi' | \hat{T} + \hat{V}_{int} + \hat{V}_{ext} | \Psi' \rangle \tag{2.16}$$

reaches its global minimum only when Ψ' is the ground-state wave function Ψ_0, with the constraint that the total number of particles is conserved. According to the first Hohenberg-Kohn theorem, Ψ' must correspond to a ground state with particle density $n'(\mathbf{r})$ and external potential $V_{ext}(\mathbf{r})$, making $E[\Psi']$ a functional of $n'(\mathbf{r})$. Applying the variational principle:

$$E[\Psi'] = \int n'(\mathbf{r}) V'_{ext}(\mathbf{r}) d(\mathbf{r}) + F[n'(\mathbf{r})] > E[\Psi_0] = \int n_0(\mathbf{r}) V_{ext}(\mathbf{r}) d(\mathbf{r}) + F[n_0(\mathbf{r})] = E[n_0(\mathbf{r})] \tag{2.17}$$

Thus, the energy functional $E[\Psi] \equiv \int n(\mathbf{r}) V_{ext}(\mathbf{r}) d(\mathbf{r}) + F[n(\mathbf{r})]$ evaluated for the correct ground-state density $n_0(\mathbf{r})$ is lower than the value of this functional for any other density $n(\mathbf{r})$. Therefore, by minimizing the total energy functional of the system with respect to variations in the density $n(\mathbf{r})$, one can find the exact ground-state density and energy. This functional, however, only determines ground-state properties and does not provide any insight into excited states.

2.3.3 Advantage and Disadvantage of Hohenberg-Kohn Theorems

The Hohenberg-Kohn theorems form the theoretical foundation of Density Functional Theory (DFT) and play a crucial role in computational chemistry and materials science. These theorems provide a significant advantage by establishing a direct relationship between the ground-state properties of many-electron systems and their electron density, thereby offering a more tractable alternative to traditional wave function-based approaches.

The first theorem demonstrates that a one-to-one correspondence exists between the ground-state electron density and the external potential acting on the system. This implies that all properties of the ground state can be described as functionals of the electron density. The second theorem introduces a variational principle, stating that the correct ground-state electron density minimizes the total energy functional [50]. This significantly reduces the complexity of quantum mechanical calculations by shifting focus from a $3N$-dimensional wave function to a three-dimensional electron density.

However, the Hohenberg-Kohn theorems also come with notable disadvantages. They are limited to ground-state properties, providing no direct insight into excited states, which poses challenges in studying electronic excitations and charge transfer processes. The effectiveness of DFT is highly dependent on the choice of exchange-correlation functional, which may not accurately capture all correlation effects, especially in systems with strong electron-electron interactions. Furthermore, while DFT is generally computationally less intensive than wave-function methods, the calculations of exchange-correlation energies can still be demanding. The reliance on external potentials and the interpretation challenges associated with electron density further highlight the limitations of the Hohenberg-Kohn theorems, necessitating careful consideration when applying DFT to complex systems.

2.3.4 Kohn-Sham Equation: Reformulating Many-Body Problems

The Kohn-Sham equation is a fundamental aspect of Density Functional Theory (DFT) that enables efficient calculations of electronic structures in many-body systems. Building on the Hohenberg-Kohn theorems, it establishes a relationship between the ground-state electron density and the external potential. The Kohn-Sham approach simplifies the many-body problem by mapping the interacting electron system onto an auxiliary system of non-interacting electrons that yield the same electron density.

In the Kohn-Sham approach, the true interacting electron system is mapped onto

an auxiliary system of non-interacting electrons that yield the same electron density as the original system. This is achieved through the Kohn-Sham equations, which can be expressed as:

$$\left[-\frac{\hbar^2}{2m}\nabla^2 + V_{eff}(\mathbf{r}) \right] \psi_i(\mathbf{r}) = \epsilon_i \psi_i(\mathbf{r}), \tag{2.18}$$

where $V_{eff}(\mathbf{r})$ is the effective potential that includes the external potential and the exchange-correlation potential. The Kohn-Sham orbitals $\psi_i(\mathbf{r})$ are used to construct the electron density $n(\mathbf{r})$ as:

$$n(\mathbf{r}) = \sum_{i}^{N} |\psi_i(\mathbf{r})|^2. \tag{2.19}$$

This approach significantly reduces the complexity of solving the many-body Schrödinger equation by allowing for the treatment of a system of independent particles, while still capturing the essential effects of electron correlation through the exchange-correlation functional.

The effective potential in the Kohn-Sham framework can be expressed as:

$$V_{eff} = V_{ext} + V_{Hartree}[n(\mathbf{r})] + V_{xc}[n(\mathbf{r})] \tag{2.20}$$

Here, V_{ext} represents the external potential acting on the electrons in the system. This potential typically arises from the interaction between the electrons and fixed nuclei or any other external fields applied to the system. In many cases, V_{ext} is described by the Coulomb potential due to the nuclei, reflecting how electrons experience attraction towards positively charged atomic cores. This term plays a crucial role in determining the overall potential landscape in which the electrons move, significantly influencing the electronic structure of the system.

The term $V_{Hartree}[n(\mathbf{r})]$ is the Hartree potential, which describes the classical electrostatic interaction between electrons in a many-body system. It accounts for the repulsion between charged particles, reflecting that the potential energy experienced

by an electron is due to the distribution of other electrons around it. The Hartree potential is calculated as:

$$V_{Hartree}[n(\mathbf{r})] = \int \frac{n(\mathbf{r})}{|\mathbf{r} - \mathbf{r}'|} d\mathbf{r}'. \tag{2.21}$$

This formulation integrates the electron density $n(\mathbf{r})'$ over all space, considering the effect of all other electrons on a given electron located at r. This approach provides a mean-field treatment of electron-electron repulsion, avoiding the complexity of considering every pair of interactions explicitly.

The exchange-correlation potential $V_{xc}[n(\mathbf{r})]$ represents the quantum mechanical effects of exchange and correlation among electrons. It is defined as:

$$V_{xc}[n(\mathbf{r})] = \frac{\delta E_{xc}[n]}{\delta n}. \tag{2.22}$$

The exchange term arises from the antisymmetry requirement of the total wave function for fermions, accounting for the reduction in energy when two electrons are spatially separated. The correlation term reflects the correlated motion of electrons that cannot be captured by a mean-field approach, accounting for the ways in which the presence of one electron affects the probability distribution of another electron's position and momentum.

From these considerations, the Kohn-Sham Hamiltonian can be formulated as:

$$\hat{H}_{KS} = -\frac{\hbar^2}{2m}\nabla^2 + V_{ext} + V_{Hartree}[n(\mathbf{r})] + V_{xc}[n(\mathbf{r})]. \tag{2.23}$$

The major distinction between the Kohn-Sham formulation and the Hartree formulation lies in the inclusion of both exchange and correlation effects in the effective potential, providing a more accurate description of many-body systems.

Solving the Kohn-Sham equation is a crucial step in density functional theory for obtaining the ground-state electron density of a many-body system. In a condensed matter system, the Kohn-Sham equation [51] provides a method to derive the exact density and energy of the ground state. The process begins with an initial electron

density n(**r**), typically a superposition of atomic electron densities. The effective Kohn-Sham potential V_{eff} is then calculated, and the Kohn-Sham equation is solved to obtain single-particle eigenvalues and wave functions. A new electron density is subsequently calculated from these wave functions.

The iterative process is generally performed numerically through self-consistent iterations, as shown in Figure 2.1 (flowchart). Self-consistency is determined by monitoring changes in total energy, electron density from the previous iteration, or the total force acting on the atoms, ensuring that these quantities fall below a specified threshold. A combination of these criteria may also be used. If self-consistency is not achieved, the electron density from the previous iteration is mixed with the current density, and the process is repeated until convergence is reached. Once the system reaches self-consistency, various properties can be calculated, such as total energy, forces, stress, eigenvalues, electron density of states, and band structure.

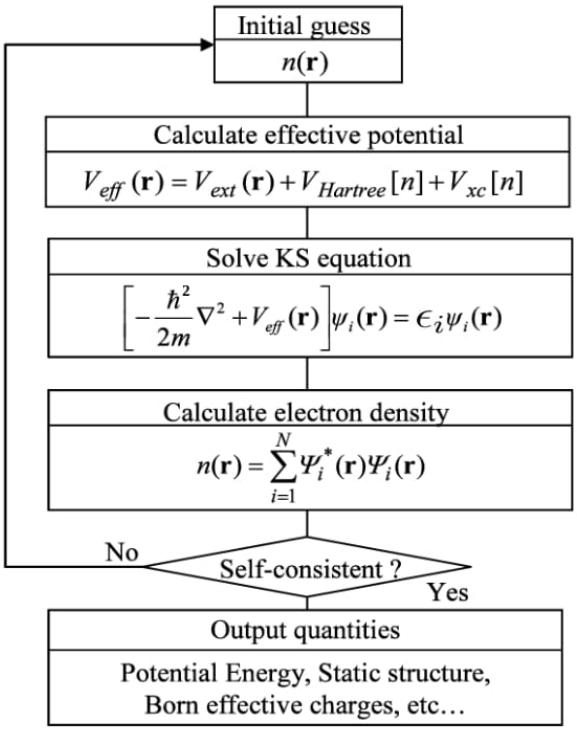

Figure 2.1: Flowchart illustrating the iterative process for solving the Kohn-Sham equation in density functional theory to obtain the ground-state electron density and associated properties of a many body system.

2.3.5 The Role and Calculation of Exchange-Correlation

In density functional theory, the exchange-correlation potential, $V_{xc}[n(\mathbf{r})]$, is a critical component that captures the complex quantum mechanical effects of electron exchange and correlation. However, V_{xc} is not derived exactly but is instead approximated due to the computational challenges of dealing with many-electron systems. One of the most common approximations is the Local Density Approximation (LDA), where V_{xc} is considered to depend solely on the local electron density. This approximation is based on the idea that in regions where the electron density is nearly uniform, the behavior of electrons can be likened to that of a homogeneous electron gas. While simple, LDA can perform reasonably well for certain materials, especially solids with nearly uniform electron densities.

To improve upon the LDA, the Generalized Gradient Approximation (GGA) introduces a dependence on the spatial gradients of the electron density. By including information about how the density changes in space, GGA provides more accurate results for systems where the density varies significantly, such as in molecules or surfaces. These improvements make GGA one of the most widely used approximations in modern DFT calculations. More advanced methods, such as hybrid functionals, combine the exchange from exact Hartree-Fock theory with the approximate exchange-correlation from LDA or GGA. Hybrid functionals, like $B3LYP$, tend to improve accuracy further, particularly for molecular systems, by including a portion of exact exchange, which LDA and GGA inherently miss.

In practice, the calculation of V_{xc} is an iterative process within the self-consistent field (SCF) method. The DFT algorithm begins with an initial guess for the electron density, usually based on atomic configurations. Using this initial density, the Kohn-Sham equations are solved to update the potential and electron density. The exchange-correlation potential, V_{xc}, is recalculated at each step based on the updated density. This process continues until the electron density converges to a self-consistent solution, meaning that the input and output densities agree within a set tolerance. Recent developments also include meta-GGA functionals, which incorporate even higher-order density-related terms, such as the kinetic energy density,

to account for more complex interactions. While computationally more expensive, these functionals can offer improved accuracy for systems with intricate electronic structures. Thus, although V_{xc} is not known exactly, various approximations—from LDA and GGA to hybrid and meta-GGA functionals—allow DFT to achieve a good balance between accuracy and computational efficiency for a wide range of materials and molecular systems.

Chapter 3

Results and Discussion

In order to explore the multifunctional behavior of the Ca_2VInO_6 double perovskite compound, a series of computational tools were employed to investigate its key physical properties include structural properties, electronic band characteristics, optical response, mechanical strength, and thermoelectric performance. Each property offers essential information regarding the compound's potential for diverse industrial and technological applications. The properties have been systematically examined using density functional theory (DFT) based calculations. We first provide a detailed description of the computational tools employed in this study and then discuss the results obtained using these tools.

3.1 Computational methods

The structural, electronic, optical, thermoelectric and mechanical properties of the Ca_2VInO_6 double perovskite are studied using the full potential linearized augmented plane wave (FP–LAPW) method, based on density functional theory method, as implemented in the WIEN2k package. To find the optimized ground states of the considered materials, the generalized gradient approximation (GGA) with the Perdew–Burke–Ernzerhof (PBE) approximation was used. However, since the

PBE–GGA method underestimates the electronic bandgap, the Tran–Blaha modified Becke–Johnson (TB–mBJ) potential was employed to achieve more accurate bandgap values, which are crucial for correctly describing the electronic and optical properties of semiconductors. The density of states and optical properties were calculated using the TB–mBJ potential. The basic functions are expended into spherical harmonic function inside the muffin-tin sphere and Furier series in the interstitial region. The value of RK_{max} was set to 8, where K_{max} is the plane wave cut-off and R_{MT} is the smallest of all atomic sphere radii. We also assigned the value of Gaussian factor G_{max} as 16 $\mathrm{Ry}^{\frac{1}{2}}$, and angular momentum vector l_{max} as 10. The energy convergence criteria was set to 10^{-5} Ry, while the charge convergence criteria was also set to 10^{-4} e, where e is an electron charge and the number of k–points in the Brillouin zone is 3500. Elastic constants and other parameters are utilized in the IRelast suite established by Murtaza for the computation of elastic properties. Finally, the Boltzmann transport equation was utilized to estimate the thermoelectric properties following the semi–classical Boltzmann transport model, as applied in BolzTraP code within the constant relaxation time approximation.

3.2 Structural properties

The double perovskite compound Ca_2VInO_6 adopts a face-centered cubic structure, belonging to the space group $Fm\bar{3}m$ (space group no: 225), with four atoms per unit cell. The conventional unit cell of Ca_2VInO_6 double perovskite is displayed in Figure 3.1. The atoms in unit cell are located as Ca at 8c(0.25, 0.25, 0.25), V at 4a(0.5, 0.5, 0.5), In at 4b(0, 0, 0) and O at 24e(0.26517, 0, 0) Wyckoff positions. In order to determine the optimized ground states of the double perovskite compound, the energy vs volume of a unit cell of the crystal was calculated based on the Birch-Murnaghan equation of states [52] which can be represented as

$$E(V) = E_0 + \frac{9V_0B_0}{10}\left\{\left[\left(\frac{V_0}{V}\right)^{2/3} - 1\right]^3 B_0' + \left[\left(\frac{V_0}{V}\right)^{2/3} - 1\right]^2 \left[6 - 4\left(\frac{V_0}{V}\right)^{2/3}\right]\right\} \tag{3.1}$$

In this equation, V_0 and V are the ground state unit cell volume and deformed unit cell volume, E_0 is the energy of the ground state, B_0 is the bulk modulus, and B_0' is its derivative. The energy vs volume optimization curve also shown in Figure 3.1, determines the ground state energy corresponding to minimum volume and from which optimized lattice constant are obtained. The optimized lattice constant are

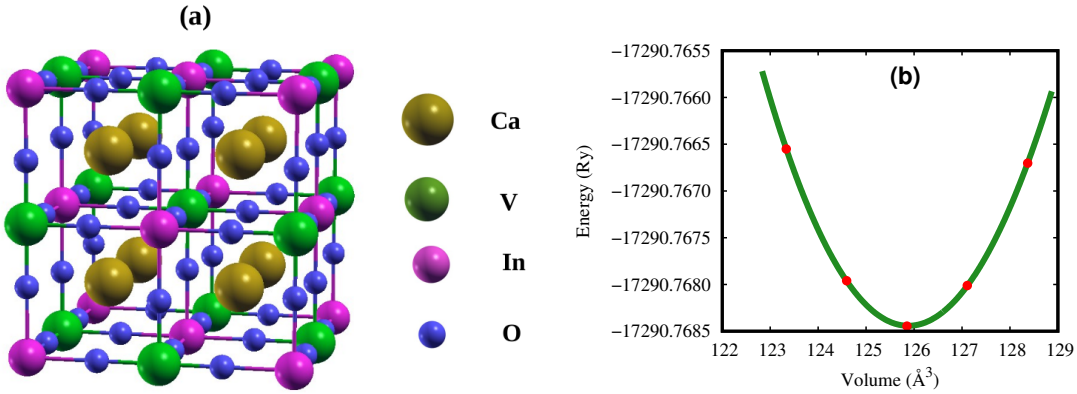

Figure 3.1: (a) Crystal structure and (b) The energy vs volume optimization curve of Ca_2VInO_6 double perovskite.

estimated to be 7.95 Å. The calculated minimum energy and corresponding volume are -17290.7684 Ry and 125.85 Å^3 respectively. we determined the optimized lattice constant for the primitive unit cell, generated the crystal structure and evaluated the total energy for the conventional unit cell.

The stability of our compound is demonstrated with tolerance factor (τ), which is defined by the following equation;

$$\tau = \frac{R_{Ca} + R_O}{\sqrt{2}\left(\frac{R_V + R_{In}}{2} + R_O\right)}$$

Where R_{Ca} , R_V, R_{In} and R_O refer to the ionic radii of Ca, V, In, O atoms respectively [53,54]. Statistical studies on the double perovskite structures conducted by Li et al. [55,56], have revealed that for a stable double perovskite, the tolerance factor τ lies within the range $0.71 < \tau < 1.00$. By using the reported ionic radii of Ca (1Å), V (0.5Å), In (0.8Å), O (1.4Å), the tolerance factor (τ) is calculated to be approximately 0.84, confirming that this compound forms a stable structure.

3.3 Electronic properties

Electronic properties of solids are very important and fundamental because of their influence on optical and thermoelectric properties. To explore the potential area for practical applications of the studied compounds, it is crucial to examine their band structure and density of states. To calculate the density of states and band structure, we employ the TB–mBJ potential, which provides a more accurate band gap compared to the PBE–GGA approximation. This is because TB–mBJ introduces a semi-local exchange potential that more effectively captures electron localization and mimics non-local exchange effects. As a result, it corrects the typical underestimation of band gaps commonly observed in standard DFT calculations. The band gap calculated with the PBE–GGA approximation is 0.836 eV, while the value obtained using the TB–mBJ approximation is 2.362 eV. We also calculated electron density for observing the bonding properties of Ca_2VInO_6. The electronic band structure, density of states and electron density are discussed in this section.

3.3.1 Band structure

The analysis of the electronic band structure leads to an understanding of the physical properties of crystalline solids, which almost completely describe both the optical and transport properties. In particular, one can categorize a solid into metal, semimetal, semiconductor or insulator by knowing band gap. The electronic band structure of Ca_2VInO_6 are presented in Figure 3.2, shifted along the high symmetry path W–L–Γ–X–W–K. The black horizontal dashed line at 0 eV indicates the Fermi level (denoted by E_F), with multiple colored lines representing the valence band (VB) and conduction band (CB) shown below and above E_F respectively. This study illustrates the band structure around the E_F ranging from -2 eV to +7 eV. According to the band structure diagram, this compound has an indirect bandgap at Γ–X because the bands lie at different symmetry points, such as the valance band maximum (VBM) at Γ–point and the conduction band minimum (CBM) at X–point with values of 2.362 eV. In the band structure valance band is closer to the Fermi level than the conduction band, which indicates that Ca_2VInO_6 exhibits $p-$ type

semiconducting behavior.

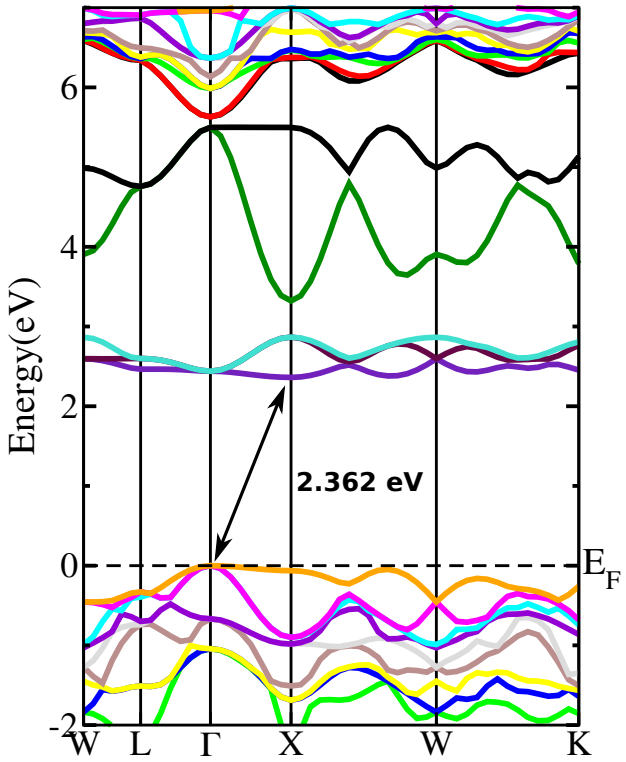

Figure 3.2: The calculated band structure of of Ca_2VInO_6 double perovskite.

3.3.2 Density of states

The density of states (DOS) represents the number of available states at a particular energy level that electrons can occupy, or the number of electron states per unit volume per unit energy. We can clarify the electronic structure by analyzing the elemental and orbital contribution from the constituent element in terms of DOS and PDOS. The calculated total and partial densities of states for Ca_2VInO_6 are displayed in Figure 3.3 and 3.4 respectively. The black vertical dashed line at 0 eV represents the Fermi level energy (E_F), while the bands formed by multiple colored lines to the left and right of E_F correspond to the valence band (VB) and conduction band (CB), respectively. From the band structure, the estimated band gap is approximately 2.362 eV, indicating that the compound exhibits semiconducting behavior. As illustrated in Figure 3.3, the total density of states (DOS) shows

slightly larger peaks in the valence band region compared to the conduction band region. This suggests that most electrons remain localized and are not free from their respective atoms. Furthermore, the contribution of electrons from O atoms to the valence band is significantly higher than that from other atoms. In contrast, electrons from v atoms contribute more prominently to the conduction band compared to electrons from the other atoms. We considered the contributions of the s,

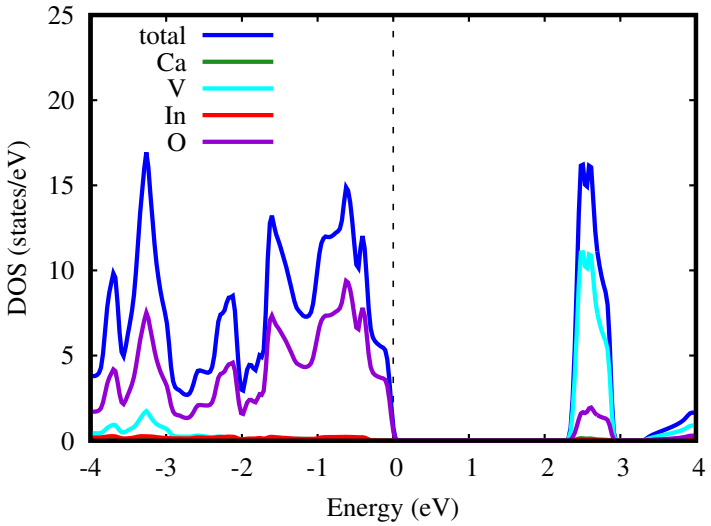

Figure 3.3: Density of states of Ca_2VInO_6 double perovskite.

p, and d orbitals for the Ca atom, the s, p, d, and f orbitals for the V and In atoms, and the s and p orbitals for the O atom. Although the overall contribution from Ca atoms is very small, Figure 3.4(a) indicates that the contribution of Ca electrons to the valence band region is greater than to the conduction band region, with notable involvement of the s, p and d orbitals. From Figure 3.4(b), we observe a highest peak is located in the conduction band, with significant peak also present in the valance band region. In the valence band, the d orbital electrons contribute most, followed by p orbital electrons. In the conduction band, however, only the d orbital electrons contribute. Figure 3.4(c) shows that most of the electrons of the In atom are in the valence band region, with the d orbital making the largest contribution, followed by the p, f, and s orbitals. Moreover, the sharpest peaks for the p and d orbital electrons appear far from the Fermi energy level. In contrast, the contribution of s orbital electrons to the conduction band is more significant than that of the other

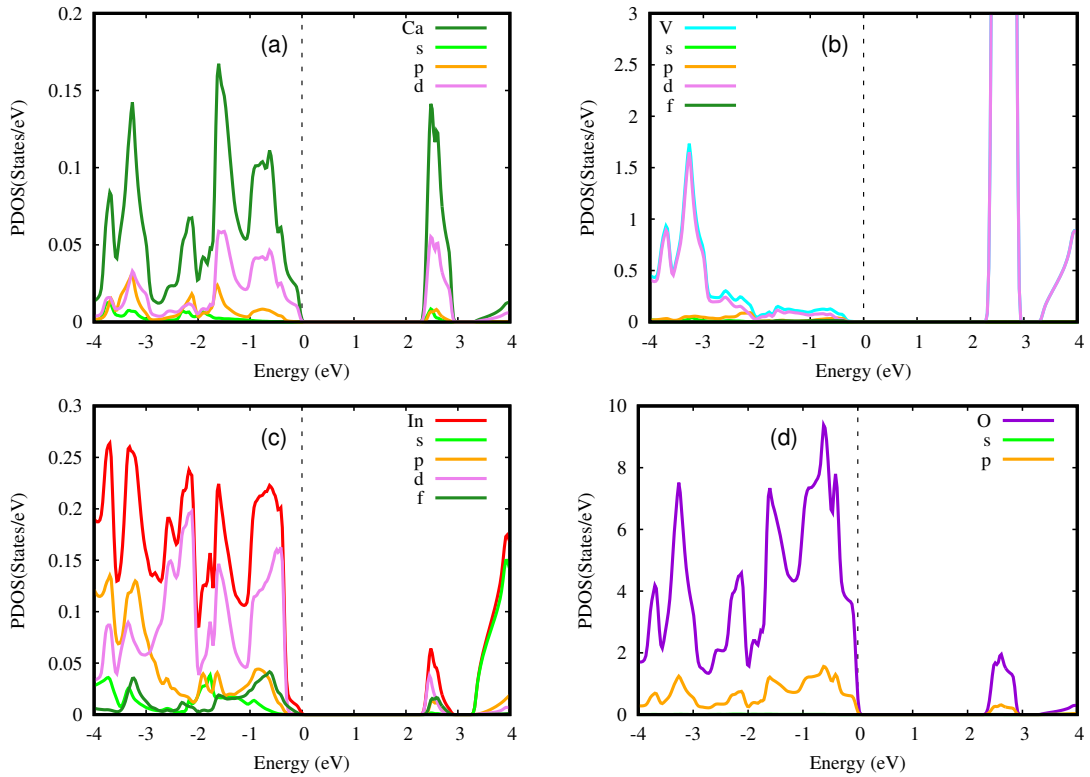

Figure 3.4: Partial density of states of (a) Ca, (b) V, (c) In and (d) O atoms for Ca_2VInO_6 double perovskite.

orbitals. Now, let's examine Figure 3.4(d) , it is evident that the electrons from the oxygen O atoms are predominantly found in the valence band, with relatively few occupying the conduction band. Additionally, the electron concentration in the p orbitals is noticeably higher than in the s orbitals.

3.3.3 Electron density

Electron density refers to the concentration or probability of finding an electron in a specific region of space, typically around an atom or molecule. Electron density and its distribution plot can be used to determine the bonding properties of compounds. Figure 3.5 illustrates the charge density along the crystallographic planes (100) and (110) for Ca_2VInO_6 , which helps in understanding the types of chemical bonding present within this double perovskite compound. Figure 3.5 reveals that along the (100) plane, the charge density distributions of Indium and Oxygen atoms exhibit no noticeable overlap, indicating the formation of an ionic bond between them. The clear separation of electron clouds suggests that In atom donates electrons to O atom,

leading to the development of In^{3+} and O^{2-} ions. This electron transfer mechanism, rather than electron sharing, confirms the ionic nature of the In—O bond. On the other hand, the charge distributions of V and O atoms slightly overlap along the (110) plane, indicating the presence of a covalent bond between these two atoms.

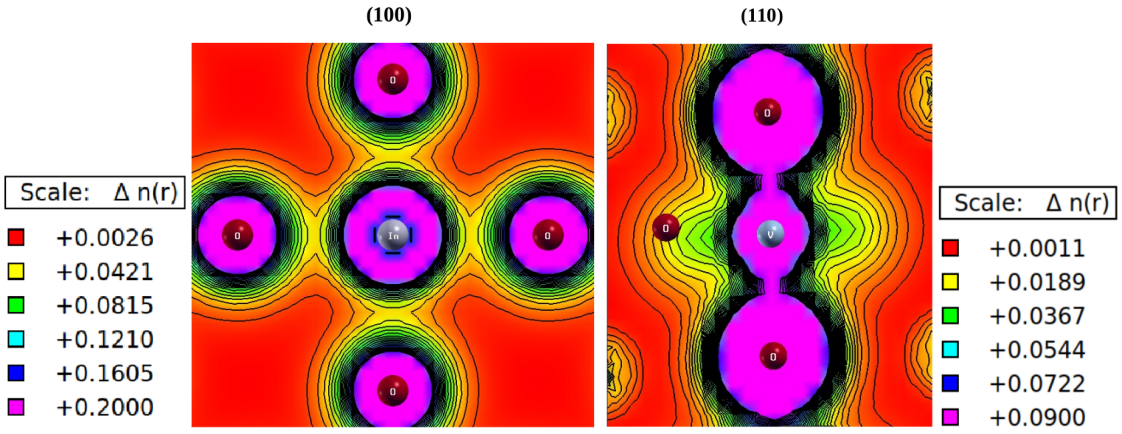

Figure 3.5: The charge density plots of Ca_2VInO_6 along (100) and (110) plane.

The observed overlap in electron density suggests that electrons are shared between V and O atoms, confirming the covalent character of the V—O bond.

3.4 Optical properties

The term optical property describes a material's behavior when electromagnetic radiation (light) is incident on the material's surface or, in other words, how a material interacts under an incident electromagnetic radiation. The optical behavior is vital for understanding the internal electronic structure of a substance, which in turn enables its effective use in photovoltaic applications, such as solar cells. We performed a detailed calculation of the different optical functions, such as dielectric function, absorption coefficient, optical conductivity, reflectivity and refractive index of Ca_2VInO_6 double perovskite in order to determine the optimum properties for solar cell devices, as well as other optoelectronic applications. All optical parameters calculated for Ca_2VInO_6 are plotted against energy ranging 0–12 eV.

3.4.1 Dielectric function

The optical nature of any material is explained by the complex dielectric function $\epsilon(\omega)$ which describes the relationship between a material's response to incident photons and its energy and is given by Ehrenreich and Cohen's equation of state as follows:

$$\epsilon(\omega) = \epsilon_1(\omega) + \mathrm{i}\epsilon_2(\omega)$$

Here, ω denotes the angular frequency of electromagnetic radiation incident on the specimen. $\epsilon_1(\omega)$ and $\epsilon_2(\omega)$ represent the real and imaginary component of the dielectric function $\epsilon(\omega)$. The real part of the dielectric function $\epsilon_1(\omega)$ describes the degree of polarization a material undergoes when exposed to electromagnetic radiation, while the imaginary part $\epsilon_2(\omega)$ reflects the material's light absorption characteristics. The imaginary part $\epsilon_2(\omega)$ of the dielectric function's is given as follows [57]:

$$\varepsilon_2(\omega) = \frac{e^2\hbar}{\pi m^2\omega^2} \sum_{v,c} \int_{\mathrm{BZ}} |M_{cv}(k)|^2 \, \delta\left(\omega_{cv}(k) - \omega\right) \, d^3k \tag{3.2}$$

where k represent the principal quantum number . The $\hbar$ is the Planck constant, ω is the angular frequency, and M is the molar mass of the carriers. The real part $\epsilon_1(\omega)$ can be determined by using the Kramers-Kronig equation [57]:

$$\varepsilon_1(\omega) = 1 + \frac{2}{\pi} P \int_0^\infty \frac{\omega' \varepsilon_2(\omega')}{\omega'^2 - \omega^2} \, d\omega' \tag{3.3}$$

Here P represent the principal quantum number. The variation of the real dielectric function $\epsilon_1(\omega)$ of Ca_2VInO_6 with the energy of the incident radiation is shown in Figure 3.6(a). The real dielectric constant of the compound is given by its static value i.e, $\epsilon_1(0)$ and found to be 4.20, indicating its strong response to electromagnetic radiation. From, Figure 3.6(a) it is also evident that $\epsilon_1(\omega)$ initially increases gradually with energy then, reaching a maximum value at 2.60 eV. After this, it decreases before reaching another peak at 4.67 eV. The peak values of $\epsilon_1(\omega)$ suggest that the compound is particularly relevant in the visible range of electromagnetic

radiation. As a result, $\epsilon_1(\omega)$ turn negative in the range of energy about 7-11 eV, so these compound exhibit metallic behavior at these energy ranges, otherwise, it is semiconductor. Figure 3.6(b) illustrates the variation of $\epsilon_2(\omega)$ with the energy of incident radiation, representing the radiation absorbed by the compound. The peak

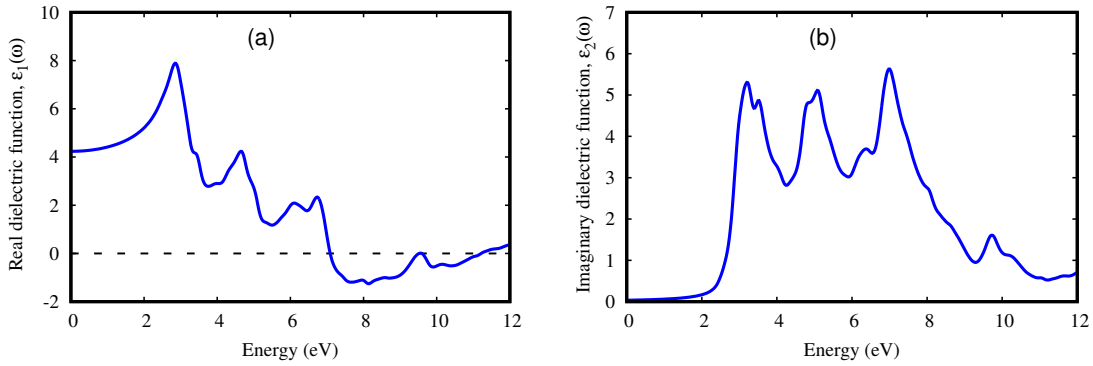

Figure 3.6: (a) Real and (b) Imaginary part of the dielectric function of Ca_2VInO_6 double perovskite.

in this curve corresponds to the transition between the maximum of the valance band and minimum of the conduction band.

3.4.2 Absorption coefficient

The absorption coefficient of a compound describes the amount of incident radiation absorbed per unit thickness. It demonstrates the efficiency of solar power conversion and indicates how far energy can penetrate into the compound before being absorbed. The absorption coefficient can be represented by the dielectric constant using the equation:

$$\alpha(\omega) = \frac{\sqrt{2\omega}}{c} \left\{ \varepsilon_1^2(\omega) + \varepsilon_2^2(\omega) - \varepsilon_1(\omega) \right\}^{\frac{1}{2}} \tag{3.4}$$

Figure 3.7 illustrates the variation of the absorption coefficient of Ca_2VInO_6 with the energy of incident radiation. The absorption process starts at a threshold energy of 2.35 eV, which is almost identical to the material's electronic bandgap. Below this threshold energy, the material remains transparent, as no absorption takes place. Visible light has a wavelength range of approximately 400 to 700 nanometers, which

corresponds to photon energies of about 1.8 to 3 eV. The absorption coefficient in the visible energy range is very low, meaning it cannot absorb visible light. However beyond this range, absorption increases, indicating a preference for absorbing ultraviolet light.

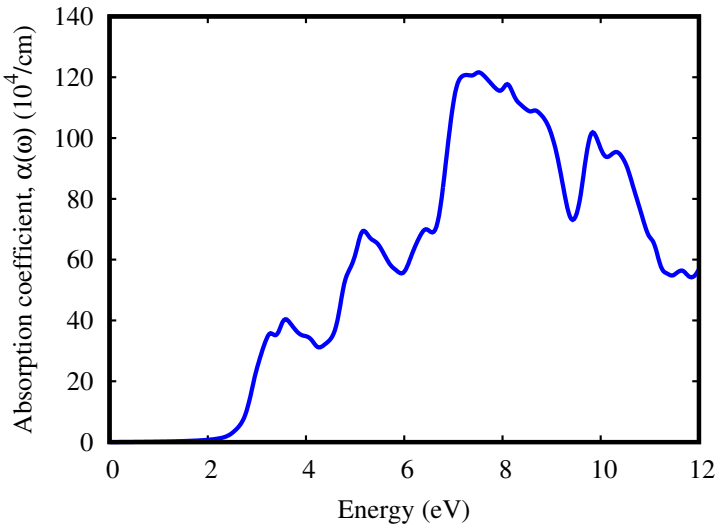

Figure 3.7: The absorption coefficient of Ca_2VInO_6 double perovskite.

3.4.3 Optical conductivity

Optical conductivity refers to the ability of a material to conduct electric current when exposed to an oscillating electric field, such as that produced by light or electromagnetic radiation. The optical conductivity exhibits features similar to the absorption spectra, as presented in Figure 3.7, because free carriers (electrons) are excited from the valence band to the conduction band when the material absorbs energy. The optical conductivity can be computed by the following equation,

$$\sigma(\omega) = \frac{\omega}{4\pi}\varepsilon_2(\omega) \tag{3.5}$$

The graphical representation of optical conductivity of Ca_2VInO_6 as a function of energy is shown in Figure 3.8. The figure demonstrates that the conductivity of the compound starts to increase once the energy exceeds the band-gap energy. This enables the material to excite electrons from the valence band (VB) to the conduction

band (CB) when it absorbs this level of energy. As a result, the conduction band gains free electrons, which facilitates electrical conductivity. The material exhibits the highest conductivity at an energy of 7.2 eV. However, after reaching 8 eV, the conductivity begins to decrease.

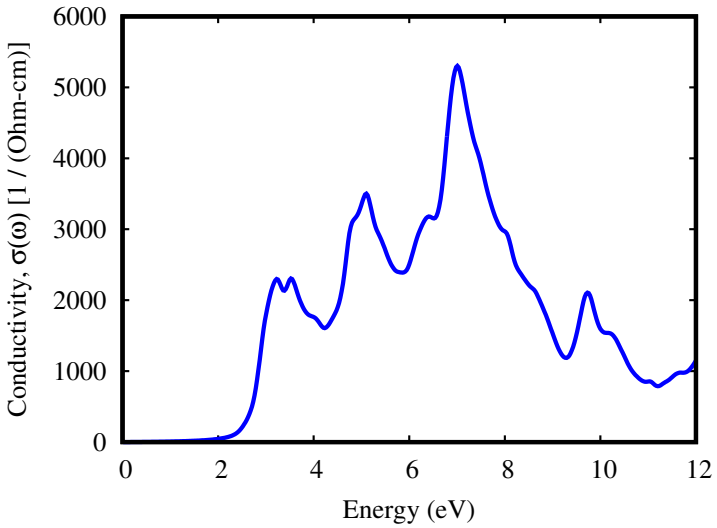

Figure 3.8: The optical conductivity of Ca_2VInO_6 double perovskite.

3.4.4 Optical reflectivity

Optical reflectivity is a measure of how much light is reflected from the surface of a material with an amount of light incident on the material. When light falls on a material results in simultaneous absorption, reflection, and transmission. For studying the reflected light from the surface, reflection coefficient $R(\omega)$ can be calculated by the equation,

$$R(\omega) = \frac{[n(\omega) - 1]^2 + k^2(\omega)}{[n(\omega) + 1]^2 + k^2(\omega)} \tag{3.6}$$

Here, n denotes the real part of the refractive index, while k represents the imaginary part of the refractive index. Figure 3.9 demonstrates the variation in $R(\omega)$ of Ca_2VInO_6 with incident radiation energy. The Figure shows that the material remains transparent below the band-gap energy. Once the energy surpasses the band-gap threshold, the optical reflectivity increases with energy and reaches a peak value at 9.1 eV in the ultraviolet region. Beyond 10 eV, the reflectivity sharply decreases,

indicating reduced reflection and a possible increase in absorption or transparenmcy at very high photon energy.

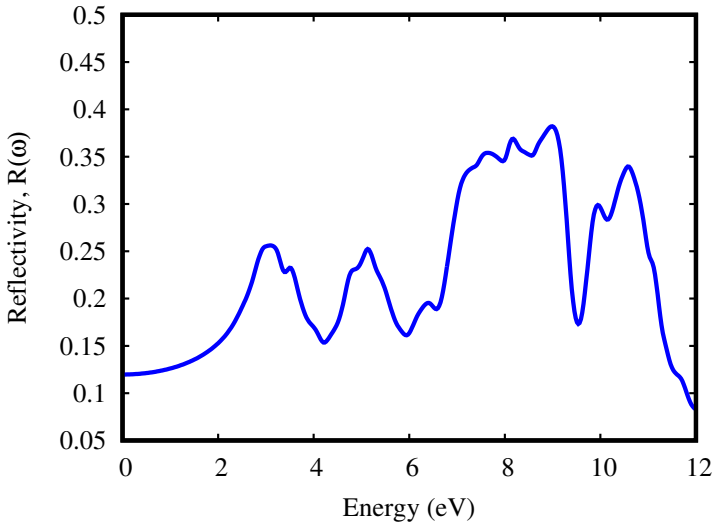

Figure 3.9: The optical reflectivity of Ca_2VInO_6 double perovskite.

3.4.5 Refractive index

The refractive index describes how much light bends and slows down when passing through a material. Higher refractive indices indicate more significant bending and slower light speeds. The refractive index and the band gap are inversly related as the refractive index rises, the bandgap falls and vice-versa. The relationship between the refractive index $n(\omega)$ as a function of frequency and the dielectric constant can be expressed by the equation,

$$n(\omega) = \frac{1}{\sqrt{2}} \left[\left(\varepsilon_1^2(\omega) + \varepsilon_2^2(\omega) \right)^{\frac{1}{2}} + \varepsilon_1(\omega) \right]^{\frac{1}{2}} \tag{3.7}$$

The refractive index vs energy curve is illustrated in Figure 3.10. From this Figure, it can be seen that in the lower energy range, there are higher values of refractive index for the compound. The refractive index increases with the increase in energy and reaches its maximum value of about $n = 2.85$ at the energy of $E = 3$ eV . After 8 eV the refractive index is continuously decreasing but never becomes negative.

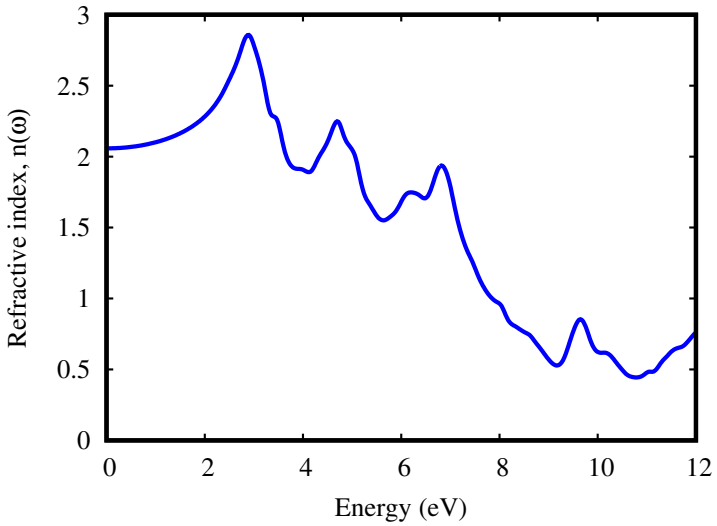

Figure 3.10: Refractive index of Ca_2VInO_6 double perovskite.

3.5 Thermoelectric properties

Thermoelectric materials have unique property of converting waste heat into electrical energy and vice versa. We have explored the thermoelectric properties of Ca_2VInO_6 double perovskite using the BoltzTrap code. Thermoelectric parameters, including Seebeck coefficient (S), figure of merit (ZT = $S^2\sigma T/\kappa$), power factor (PF = $\sigma S^2/\tau$), electrical conductivity (σ/τ) and thermal conductivity (κ_e/τ), were calculated as a function of temperature ranging from 100K to 1000K were calculated. Here, τ indicates relaxation time having a constant value 10^{-14}s. The Seebeck coefficient (S) is defined as the ratio of the voltage produced (∇V) to the temperature gradient (∇T), which can be expressed mathematically as $S = \nabla V/\nabla T$. Seebeck coefficient (S) plotted against temperature as shown in Figure 3.11(a). The Seebeck coefficient decreases as carrier concentration increases, as demonstrated by the formula below [58, 59].

$$S = \frac{8\pi^2 k_B^2}{3eh^2}\left(\frac{\pi}{3n}\right)^{\frac{2}{3}} m^* T$$

Where, k_B is the Boltzmann constant, e is the charge of an electron, h is Planck's constant, n is the carrier concentration, m^* is the effective mass of the charge carriers, and T is the temperature. At room temperature, the Seebeck coefficient is recorded as 310 μV K^{-1}. The reduction in the value of S with temperature is due to annulment of induced Seebeck voltage because of the drift of charge carriers.

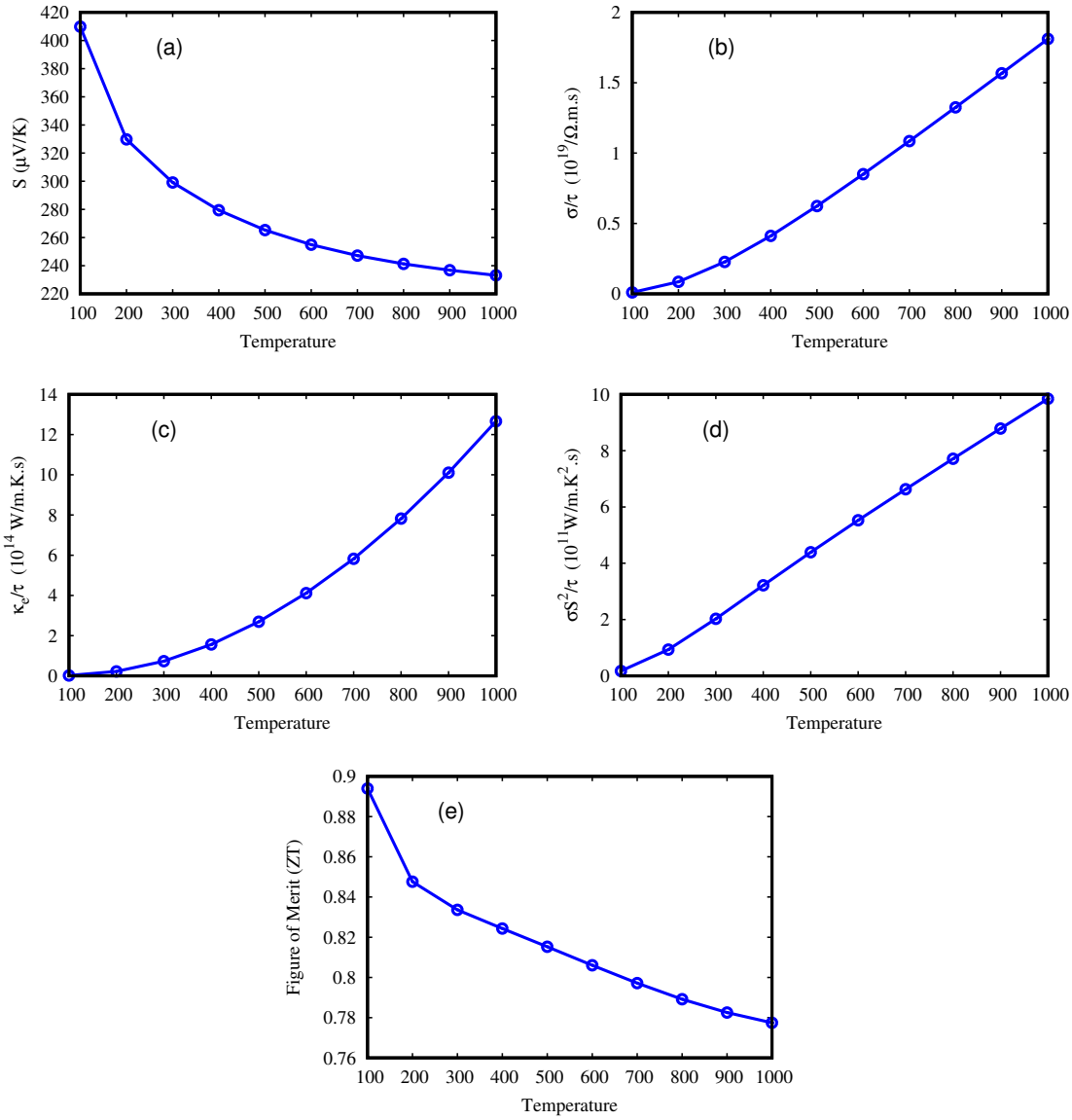

Figure 3.11: Thermoelectric properties as (a) Seebeck coefficient (S), (b) Electrical conductivity (σ/τ), (c) Thermal conductivity (κ_e/τ), (d) Power factor ($\sigma S^2/\tau$) and (e) Figure of merit (ZT) of Ca_2VInO_6 double perovskite.

The positive value of S for Ca_2VInO_6 suggests that positive charge carriers are the majority charge carriers in the material, confirming its p–type semiconducting behavior. The mobility of charge carriers is determined from the electrical conductivity. The electrical conductivity as a function of temperature is displayed in Figure 3.11(b). The calcualted results reveal a linear increase in σ/τ with increasing temperature. This also implies a decrease in electrical resistivity with rising temperature, indicating a negative temperature coefficient of resistivity, which supports the semiconductor nature of the studied compound. Thermal conductivity is

a key factor in determining the thermoelectric performance of a material, as it governs the heat transport mechanisms contributed by both electrons and phonons. In the BoltzTraP code, the contribution of phonons to thermal conductivity is considered negligible. Therefore, Figure 3.11(c) presents the material's electronic thermal conductivity (κ_e/τ) as a function of temperature. This Figure shows that as temperature increases, the ability of the compound to conduct heat through electrons improves significantly, making it highly suitable for high temperature electronic application. The performance of thermoelectric material is also analyzed by power factor. The temperature–dependent variation of PF is shown in Figure 3.11(d). Power factor increases with an increase of temperature, which demonstrates the suitability of this studied compound for high temperature application. Most important among the thermoelectric parameters is the figure of merit (ZT). Figure of merit (ZT), a dimensionless quantity, is a measure of the conversion efficiency of thermoelectric material. The thermoelectric material having ZT closer or equal to one are accepted as appropriate material or thermoelectric device application. It can be noted from Figure 3.11(e) that the value of ZT decreases as the temperature increases. As observed at high temepratures, the bandgap reduces, so the value of ZT is also reduced. The highest value of ZT are observed as 0.89 at 100K which is closer to unity make this studied compound very attractive for thermoelectric device application.

3.6 Mechanical properties

The mechanical performance of the investigated compound was evaluated by calculating its elastic parameters. Since Ca_2VInO_6 has a cubic crystalline structure, only the elastic constants C_{11}, C_{12} and C_{44} are necessary to analyze its mechanical properties. The mechanical stability of a crystal is determined by its elastic constants, following the Born criteria, which can be expressed as follows: C_{11} - $C_{12} > 0$, $C_{11} > 0$, $C_{44} > 0$, $C_{11} + 2C_{12} > 0$, $C_{12} < \mathrm{B} < C_{11}$. Here, C_{11} represents the longitudinal elastic constant, which describes elasticity along the axis, while C_{12} and C_{44} are shear elastic constants, characterizing elasticity in shear deformation. Table

3.1 shows that Ca_2VInO_6 is mechanically stable as satisfies the above Born stability criteria. Cauchy pressure indicates whether a compound is brittle or ductile. A negative value suggests brittleness, while a positive value indicates ductility. As shown in Table 3.1, the positive Cauchy pressure for Ca_2VInO_6 confirms its ductile nature. The mechanical properties, including the Bulk modulus (B), Shear modulus (G),

C_{11}	C_{12}	C_{44}	C_{12} - C_{44}	B	G	Y	A	B/G	ν
259.80	95.39	81.86	13.53	150.19	81.99	208.12	0.99	1.83	0.27

Table 3.1: The computed values of elastic constant C_{11}, C_{12}, C_{44}, Cauchy's pressure, Bulk modulus (B), Shear modulus (G), Young's modulus (Y), Anisotrophy factor (A), Pugh ratio (B/G) and Poisson's ratio (ν) of Ca2VInO6.

Young's modulus (Y), Pugh's ratio (B/G), Poisson's ratio (ν), as well as Anisotrophy factor (A) of the cubic Ca_2VInO_6 double perovskite have been determined from the estimated elastic constants and are presented in Table 3.1. The bulk and shear moduli that can forecast the hardness of material can be found using the Viogt-Reuss-Hill averaging scheme approach [60]. The Viogt limits of the bulk modulus (B) and shear modulus (G) for the cubic system are as follows:

$$B_v = \frac{C_{11} + 2C_{12}}{3} \tag{3.8}$$

$$G_v = \frac{C_{11} - C_{12} + 3C_{44}}{5} \tag{3.9}$$

However, the Reuss formulae for the bulk and shear moduli are:

$$B_v = B_R \tag{3.10}$$

$$G_R = \frac{5(C_{11} - C_{12})C_{44}}{4C_{44} + 3(C_{11} - C_{12})} \tag{3.11}$$

Using Hill's average approximation the bulk and shear moduli are defined as;

$$B = \frac{B_v + B_R}{2} \tag{3.12}$$

$$G = \frac{G_v + G_R}{2} \tag{3.13}$$

Young's modulus, determines the strength of material is ratio of linear stress and strain can be evaluated via relation.

$$Y = \frac{9BG}{3B + G} \tag{3.14}$$

Pugh's ratio is a key indicator of a material's ductile or brittle nature. According to the Pugh's criterion, if $B/G > 1.75$, the material is considered as a ductile material; otherwise, it is brittle. For Ca_2VInO_6, the calculated ratio is 1.83, which points to its ductile nature. Poisson's ratio index (ν) also helps to assess ductility or brittleness. A critical Poisson's ratio value of 0.26 distinguishes ductile from brittle materials. If ν is greater than 0.26, the material is ductile; otherwise, it is brittle. The studied material exhibits ductile behavior with a ν value of 0.27. Anisotropy is a crucial factor that describes a material's directional properties. It can be calculated by the relation;

$$A = \frac{2C_{44}}{C_{11} - C_{12}} \tag{3.15}$$

Whether a material is isotropic or anisotropic is determined by its anisotropy factor (A). When A is greater than 1, it indicates significant anisotropy, with varying stiffness in different crystallographic directions. If A is less than 1, the material is still anisotropic, but the elastic stiffness varies differently with direction. An A value of 1 represents a perfectly isotropic material. Ca_2VInO_6 is identified as an isotropic double perovskite compound, as its anisotropy factor of 0.99 is nearly equal to 1.

Chapter 4

Summery

The structural, elastic, electronic, optical and thermoelectric properties of Ca_2VInO_6 double perovskite have been studied using DFT calculations. For its most stable structure, the lattice constant found to be 7.95 Å. The analysis of mechanical properties confirms that Ca_2VInO_6 is ductile in nature and mechanically stable, with a value of Poisson's ratio is 0.27 and Pugh's ratio is 1.83. According to electronic analysis, Ca_2VInO_6 exhibit p–type semiconducting behavior with indirect bandgap of 2.362 eV. The electron density aids in understanding the chemical bonding in Ca_2VInO_6, maintaining ionic and covalent bonds In–O and V–O, respectively. The optical properties show interesting phenomena with highest optical absorption in the ultraviolet region and that's why our studied compound is suitable for optoelectronic devices such as UV Photodetectors, Light-Emitting Diodes and Photovoltaic devices. Furthermore, the thermoelectric characteristics of the material are quite interesting and exhibit a high figure of merit that is 0.89, which describes its potential for thermoelectric generators.

Bibliography

[1] Naci Kalkan, E.A. Young, and Ahmet Celiktas. Solar thermal air conditioning technology reducing the footprint of solar thermal air conditioning. *Renewable and Sustainable Energy Reviews*, 16(8):6352–6383, 2012.

[2] Alireza Khaligh and Omer C Onar. *Energy harvesting: solar, wind, and ocean energy conversion systems*. CRC press, 2017.

[3] Mohammed Ismael. Ferrites as solar photocatalytic materials and their activities in solar energy conversion and environmental protection: A review. *Solar Energy Materials and Solar Cells*, 219:110786, 2021.

[4] Hanbee Lee, Zhi Jiang, Tomoyuki Yokota, Kenjiro Fukuda, Sungjun Park, and Takao Someya. Stretchable organic optoelectronic devices: Design of materials, structures, and applications. *Materials Science and Engineering: R: Reports*, 146:100631, 2021.

[5] Huanping Zhou, Qi Chen, Gang Li, Song Luo, Tze-bing Song, Hsin-Sheng Duan, Ziruo Hong, Jingbi You, Yongsheng Liu, and Yang Yang. Interface engineering of highly efficient perovskite solar cells. *Science*, 345:542–546, 2014.

[6] Julian Burschka, Norman Pellet, Soo-Jin Moon, Robin Humphry-Baker, Peng Gao, Mohammad K Nazeeruddin, and Michael Grätzel. Sequential deposition as a route to high-performance perovskite-sensitized solar cells. *Nature*, 499:316–319, 2013.

[7] Andrew Barnabas Wong, Minliang Lai, Samuel Wilson Eaton, Yi Yu, Elbert Lin, Letian Dou, Anthony Fu, and Peidong Yang. Growth and anion exchange conversion of CH_3NHPbX_3 nanorod arrays for light-emitting diodes. *Nano Letters*, 15:5519–5524, 2015.

[8] Erjin Zheng, Brian Yuh, Gabriella A Tosado, and Qiuming Yu. Solution-processed visible-blind uv-a photodetectors based on $CH_3NH_3PbCl_3$ perovskite thin films. *Journal of Materials Chemistry C*, 5:3796–3806, 2017.

[9] Christopher Eames, Jarvist M. Frost, Piers R.F. Barnes, Brian C. O'regan, Aron Walsh, and M. Saiful Islam. Ionic transport in hybrid lead iodide perovskite solar cells. *Nature Communications*, 6:7497, 2015.

[10] Sanjay Pachori, Rohit Agarwal, Akash Shukla, Upasana Rani, and A. Verma. Mechanically stable with highly absorptive formamidinium lead halide perovskites [$(HC(NH_2)_2PbX_3$; X = Br, Cl]: Recent advances and perspectives. *International Journal of Quantum Chemistry*, 121, 04 2021.

[11] Guichuan Xing, Nripan Mathews, Shuangyong Sun, Swee Sien Lim, Yeng-Ming Lam, Michael Graetzel, Subodh Mhaisalkar, and Tze Chien Sum. Long-range balanced electron- and hole-transport lengths in organic-inorganic $CH_3NH_3PbI_3$. *Science (New York, N.Y.)*, 342:344–347, 10 2013.

[12] Kyle Frohna, Tejas Deshpande, John Harter, Wei Peng, Bradford A. Barker, Jeffrey B. Neaton, Steven G. Louie, Osman M. Bakr, David Hsieh, and Marco Bernardi. Inversion symmetry and bulk rashba effect in methylammonium lead iodide perovskite single crystals. *Nature Communications*, 9(1), 05 2018.

[13] Giacomo Giorgi, Jun-Ichi Fujisawa, Hiroshi Segawa, and Koichi Yamashita. Small photocarrier effective masses featuring ambipolar transport in methylammonium lead iodide perovskite: a density functional analysis. *The Journal of Physical Chemistry Letters*, 4(24):4213–4216, 2013.

[14] Bing Xiao Jing Feng. Effective masses and electronic and optical properties of nontoxic $MASnX_3$ (X = Cl, Br, and I) perovskite structures as solar cell absorber: A theoretical study using $HSE0_6$. *American Chemical Society Journals*, 118(34):19655–19660, 2014.

[15] Upasana Rani, Peeyush Kamlesh, Rohit Agrawal, Akash Shukla, and A. Verma. Emerging study on lead-free hybrid double perovskite $(CH_3NH_3)_2AgInBr_6$: Potential material for energy conversion between heat and electricity. *Energy Technology*, 10, 07 2022.

[16] Yashaswi Soni, Upasana Rani, Akash Shukla, Tarun Kumar Joshi, and Ajay Singh Verma. Transition metal-based halides double Cs_2ZSbX_6 (Z =

Ag, Cu, and X = Cl, Br, I) perovskites: A mechanically stable and highly absorptive materials for photovoltaic devices. *Journal of Solid State Chemistry*, 314:123420, 2022.

[17] Upasana Rani, Peeyush Kamlesh, Rohit Agarwal, Jyoti Kumari, and A. Verma. Electronic and thermo-physical properties of double antiperovskites X_6SOA_2 (X = Na, K and A = Cl, Br, I): A non-toxic and efficient energy storage materials. *International Journal of Quantum Chemistry*, 121, 06 2021.

[18] Md. Zahidur Rahaman and A. K. M. Akther Hossain. Effect of metal doping on the visible light absorption, electronic structure and mechanical properties of non-toxic metal halide $CsGeCl_3$. *RSC Adv.*, 8:33010–33018, 2018.

[19] K.C. Bhamu, Amit Soni, and Jagrati Sahariya. Revealing optoelectronic and transport properties of potential perovskites Cs_2PdX_6 (X = Cl, Br): A probe from density functional theory (DFT). *Solar Energy*, 162:336–343, 2018.

[20] Long Zhang, Yuanyuan Fang, Laizhi Sui, Jiejuan Yan, Kai Wang, Kaijun Yuan, Wendy L. Mao, and Bo Zou. Tuning emission and electron–phonon coupling in lead-free halide double perovskite $Cs_2AgBiCl_6$ under pressure. *ACS Energy Letters*, 4(12), 11 2019.

[21] Eric T. McClure, Molly R. Ball, Wolfgang Windl, and Patrick M. Woodward. Cs_2AgBiX_6 (X = Br, Cl): New visible light absorbing, lead-free halide perovskite semiconductors. *Chemistry of Materials*, 28(5):1348–1354, 2016.

[22] Jun Zhou, Ximing Rong, Maxim S. Molokeev, Xiuwen Zhang, and Zhiguo Xia. Exploring the transposition effects on the electronic and optical properties of $Cs_2AgSbCl_6$ via a combined computational-experimental approach. *J. Mater. Chem. A*, 6:2346–2352, 2018.

[23] Yehonadav Bekenstein and A. Paul Alivisatos. Probing the stability and band gaps of $Cs_2AgInCl_6$ and $Cs_2AgSbCl_6$ lead-free double perovskite nanocrystals. *Chemistry of Materials*, 31(9):3134–3143, apr 2019.

[24] Cuncun Wu, Qiaohui Zhang, Yang Liu, Wei Luo, Xuan Guo, Ziru Huang, Hungkit Ting, Weihai Sun, Xinrui Zhong, Shiyuan Wei, Shufeng Wang, Zhijian Chen, and Lixin Xiao. The dawn of lead-free perovskite solar cell: Highly stable double perovskite $Cs_2AgBiBr_6$ film. *Advanced Science*, 5(3):1700759, 2018.

[25] Gonzalo García-Espejo, Daily Rodríguez-Padrón, Rafael Luque, Luis Camacho, and Gustavo de Miguel. Mechanochemical synthesis of three double perovskites: $Cs_2AgBiBr_6$,$(CH_3NH_3)_2TlBiBr_6$ and $Cs_2AgSbBr_6$. *Nanoscale*, 11:16650–16657, 2019.

[26] Ying Liu, Angshuman Nag, Liberato Manna, and Zhiguo Xia. Lead-free double perovskite $Cs_2AgInCl_6$. *Angewandte Chemie International Edition*, 60(21):11592–11603, 2021.

[27] Nada T. Mahmoud, Jamil M. Khalifeh, Ahmad A. Mousa, Hassan K. Juwhari, and Bothina A. Hamad. The energetic, electronic and magnetic structures of $Fe_{2-x}Co_xVSn$ alloys: Ab-initio calculations. *Physica B: Condensed Matter*, 430:58–63, 2013.

[28] Nada T. Mahmoud, Bayan R. Almalaji, Ahmad A. Mousa, and Jamil M. Khalifeh. Effect of the"3-d" band filling on the structural, electronic, magnetic and optical properties of $TMScO_3$ perovskite. *Chinese Journal of Physics*, 65:500–512, 2020.

[29] Nada T. Mahmoud, Jamil M. Khalifeh, and Ahmad A. Mousa. Ab-initio investigations of the structural, electronic, magnetic and optical properties of $Ca_{1-x}Eu_xLiF_3$ fluoroperovskite. *Computational Condensed Matter*, 21:e00432, 2019.

[30] Nada T. Mahmoud, Jamil M. Khalifeh, and Ahmad A. Mousa. Effects of rare earth element eu on structural, electronic, magnetic, and optical properties of fluoroperovskite compounds $SrLiF_3$: First principles calculations. *Physica B: Condensed Matter*, 564:37–44, 2019.

[31] Nada T. Mahmoud, Ahmad A. Mousa, and Adel A. Shaheen. Effect of doping titanium ions on semi-conducting behavior, photovoltaic, and thermoelectric perovskite-type oxides VScTiO: Ab-inito study. *International Journal of Energy Research*, 46(9):12184–12206, 2022.

[32] G Murtaza. Investigation of the lead-free double perovskites Cs_2AgSbX_6 (X= Cl, Br, I) for optoelectronic and thermoelectric applications. *arXiv preprint arXiv:2008.06384*, 2020.

[33] Sidra Khatoon, Satish Kumar Yadav, Vishwadeep Chakravorty, Jyotsna Singh, Rajendra Bahadur Singh, Md Saquib Hasnain, and S.M. Mozammil Hasnain.

Perovskite solar cell's efficiency, stability and scalability: A review. *Materials Science for Energy Technologies*, 6:437–459, 2023.

[34] Muhammad Faizan, Xinjiang Wang, Shaimaa AM Abdelmohsen, KC Bhamu, Subrahmanyam Sappati, Amel Laref, Nisar Muhammad, Muhammad Mushtaq, Ashraf MM Abdelbacki, and Rabah Khenata. Understanding the electronic structure and optical properties of vacancy-ordered double perovskite $A2BX_6$ for optoelectronic applications. *Energy & Fuels*, 36(13):7065–7074, 2022.

[35] Muhammad Zafarullah Kazim, Muhammad Yaseen, Shatha A. Aldaghfag, Mudassir Ishfaq, Mubashar Nazar, Misbah, Muhammad Zahid, and R. Neffati. DFT study of optoelectronic and thermoelectric properties of cubic Ba_2ZrMO_6(M = Ce, Ti) double perovskites. *Journal of Solid State Chemistry*, 315:123419, 2022.

[36] Asima Aziz, Shatha A. Aldaghfag, Muhammad Zahid, Javed Iqbal, Misbah, Muhammad Yaseen, and H.H. Somaily. Theoretical investigation of X_2NaIO_6 (X= Pb,Sr) double perovskites for thermoelectric and optoelectronic applications. *Physica B: Condensed Matter*, 630:413694, 2022.

[37] Samah Al-Qaisi, Malak Azmat Ali, Tahani A. Alrebdi, Tuan V. Vu, Manal Morsi, Bakhtiar Ul Haq, R. Ahmed, Q. Mahmood, and Sohail Afzal Tahir. First-principles investigations of Ba_2NaIO_6 double perovskite semiconductor: Material for low-cost energy technologies. *Materials Chemistry and Physics*, 275:125237, 2022.

[38] Saveer Ahmad Khandy, S. Yousuf, T. M. Bhat, S. Singh, S. A. Sofi, S. A. Mir, Ab. Q. Seh, M. Nabi, N. A. Ganie, A. Rasool, R. A. Mir, P. Kumar, and D. C. Gupta. Forecasting electronic-band structure and magnetism in complex double perovskite Ba_2CdReO_6. *AIP Conference Proceedings*, 2265(1):030359, 11 2020.

[39] P. Blaha, Karlheinz Schwarz, P. Sorantin, and S.B. Trickey. Blaha, P., Schwarz, K., Sorantin, P. Trickey, S.B. Full-potential, linearized augmented plane wave programs for crystalline systems. Comput. Phys. Commun. 59, 399-415. *Computer Physics Communications*, 59:399–415, 06 1990.

[40] Peter Blaha, Karlheinz Schwarz, Fabien Tran, Robert Laskowski, Georg K. H. Madsen, and Laurence D. Marks. WIEN2k: An APW+lo program for calculat-

ing the properties of solids. *The Journal of Chemical Physics*, 152(7):074101, 02 2020.

[41] D.J. Griffiths and D.F. Schroeter. *Introduction to Quantum Mechanics*. Cambridge University Press, 2018.

[42] Max Born. Quantenmechanik der stoßvorgänge. *Zeitschrift für Physik*, 38(11):803–827, 1926.

[43] Georg K.H. Madsen and David J. Singh. Boltztrap. a code for calculating band-structure dependent quantities. *Computer Physics Communications*, 175(1):67–71, July 2006.

[44] D.J. Griffiths and D.F. Schroeter. *Introduction to Quantum Mechanics*. Cambridge University Press, 2018.

[45] Robert G Parr and Yang Weitao. Density-functional theory of atoms and molecules. 01 1995.

[46] Klaus Capelle. A birds-eye view of density-functional theory. *Brazilian Journal of Physics*, 2006.

[47] M.P. Marder. *Condensed Matter Physics*. Wiley, 2015.

[48] W. Koch and M.C. Holthausen. *A Chemist's Guide to Density Functional Theory*. Wiley, 2015.

[49] P. Hohenberg and W. Kohn. Inhomogeneous electron gas. *Phys. Rev.*, 136:B864–B871, Nov 1964.

[50] Stefaan Cottenier. Density functional theory and the family of LAPW-methods: a step-by-step introduction. 2004.

[51] W. Kohn and L. J. Sham. Self-consistent equations including exchange and correlation effects. *Physical Review*, 140(4A):1133–1138, November 1965.

[52] Francis Birch. Finite strain isotherm and velocities for single-crystal and polycrystalline nacl at high pressures and 300°k. *Journal of Geophysical Research: Solid Earth*, 83(B3):1257–1268, 1978.

[53] Yao Cai, Wei Xie, Yin Ting Teng, P. C. Harikesh, Biplab Ghosh, Patrick Huck, Kristin A. Persson, Nripan Mathews, Subodh G. Mhaisalkar, Matthew Sherburne, and Mark Asta. High-throughput computational study of halide double

perovskite inorganic compounds. *Chemistry of Materials*, 31(15):5392–5401, 2019.

[54] Edson Meyer, Dorcas Mutukwa, Nyengerai Zingwe, and Raymond Taziwa. Lead-free halide double perovskites: A review of the structural, optical, and stability properties as well as their viability to replace lead halide perovskites. *Metals*, 8:667, 08 2018.

[55] Chonghe Li, Kitty Chi Kwan Soh, and Ping Wu. Formability of ABO_3 perovskites. *Journal of Alloys and Compounds*, 372(1):40–48, 2004.

[56] Chong Li, Weizhong Ding, Liming Feng, Yonghui Gao, and Ziming Guo. Formability of ABX_3 (X = F, Cl, Br, I) halide perovskites. *Acta Crystallographica Section B*, 64:702–707, 11 2008.

[57] Peter Blaha, Karlheinz Schwarz, Georg K H Madsen, Dieter Kvasnicka, Joachim Luitz, Robert Laskowsk, Fabien Tran, Laurence Marks, and Laurence Marks. *WIEN2k: An Augmented Plane Wave Plus Local Orbitals Program for Calculating Crystal Properties*. Techn. Universitat, 2019.

[58] Chong Xiao, Zhou Li, Kun Li, Pengcheng Huang, and Yi Xie. Decoupling interrelated parameters for designing high performance thermoelectric materials. *Accounts of chemical research*, 47, 02 2014.

[59] Gang Zhou and Dong Wang. Few-quintuple bi_2te_3 nanofilms as potential thermoelectric materials. *Scientific Reports*, 5(1):8099, 2015.

[60] H. B. Huntington. The elastic constants of crystals. In *Solid State Physics*, volume 7, pages 213–351. Academic Press, 1958.